

pubs.acs.org/acscatalysis Research Article

Tuning CO₂RR Pathways through Water Control in Ionic Liquids

Primaggio S. Mantovi, Jean C. da Cruz, Leonardo D. De Angelis, Maykon L. Souza, Liane M. Rossi, Susana I. Córdoba de Torresi, Fabio H. B. Lima, and Roberto M. Torresi*



Cite This: ACS Catal. 2025, 15, 18261-18269



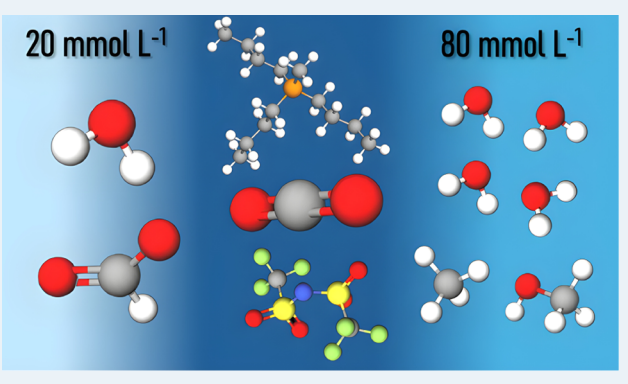
ACCESS I

Metrics & More

Article Recommendations

s Supporting Information

ABSTRACT: The electrochemical reduction of CO₂ (CO₂RR) into value-added chemicals offers a compelling route toward fuel and chemical production. In this study, the influence of water concentration on CO₂RR performance is explored using a Cu/ Cu₂O catalyst interfaced with a CO₂-philic ionic liquid (IL), methyltributylphosphonium bis(trifluoromethylsulfonyl)imide (P₁₄₄₄TFSI). Catalyst characterization prior to electrolysis confirmed the presence of the Cu₂O (111) facet and Cu⁺ surface species, which remained on the surface even after electrolysis. This does not normally occur with aqueous electrolytes, which typically reduce almost all the oxide during the initial stages of electrolysis. Electrochemical tests across different water concentrations (<1-80 mmol L⁻¹) demonstrated that water modulates both proton



availability and surface composition. At 20 mmol L⁻¹, CO₂RR selectivity shifted toward formate/formic acid (86% of product distribution) with suppressed methanol production, suggesting that the inhibition of the *CHO pathway and the promotion of *CO intermediates is favorable for C–C coupling. In contrast, 80 mmol L^{-1} water enables the *CHO pathway, yielding methanol and methane. At highly negative potentials (-1.3 to -1.6 V vs Fc/Fc⁺), extended hydrocarbon products, including propylene and butane, emerged, enabled by stabilized *C₂ intermediates and the wide electrochemical stability window of the IL. Butane formation was attributed to ethylene dimerization, independent of *H coverage, and the formation of propylene indicates that C-C coupling can occur among three intermediates that originate from *CO. Faradaic efficiencies for hydrogen remained low throughout, especially at 20 mmol L⁻¹, affirming HER suppression by the IL. Importantly, the IL showed no signs of degradation postelectrolysis. This work highlights the pivotal role of water in tuning CO₂RR selectivity and reaction pathways, demonstrating that careful control of proton donors in nonaqueous environments enables tailored hydrocarbon formation via stabilized intermediates and the mechanistic steering of complex multicarbon reactions.

KEYWORDS: CO2 reduction reaction, ionic liquid, electrocatalysis, phosphonium ionic liquids, water control

INTRODUCTION

During the past few decades, greenhouse gas emissions have noticeably increased, with CO₂ emerging as one of the most concerning contributors; the CO₂ concentration in the atmosphere has reached approximately 430 ppm. Over the past century, numerous strategies have been developed to capture and convert CO2 into valuable chemicals, including methanol, carbon monoxide, ethylene, and various other potential products.^{2–7} Electrocatalysis is a promising technique for addressing this challenge, as it can be carried out under ambient pressure and temperature conditions.8

In terms of electrocatalysts, copper-based electrodes are one of the few that can produce larger molecules. Metallic Cu is a unique catalyst for the CO₂RR because of its intermediary binding energy with *CO, which is the key intermediate for C₂₊ production due to a dimerization step needed to grow carbon chains. 10 It can also be prepared with different preferentially exposed facets, in which the (111) facet is more chemically stable and predominantly yields methane and

methanol.2 This finding highlights the importance of controlling which facet is exposed during the CO2RR, leading to different reaction mechanisms and modifying the catalyst stability. 11,12 Furthermore, compared with electropolished Cu, Cu₂O-derived catalysts exhibit higher activity toward the CO₂RR because of the creation of transient active sites due to superficial defects and irregular edges during reduction, 13 lower activation energy for the transition state of the ratedetermining step,¹⁴ and the presence of residual subsurface oxygen.^{15–19} On this basis, a well-established methodology was employed to synthesize Cu₂O (111) electrodeposited films, a

Received: July 17, 2025 Revised: October 10, 2025 Accepted: October 13, 2025



highly active precursor material for converting CO_2 into valuable products. $^{20-23}$

With respect to the electrolyte, a key reagent for the CO₂RR is water, which serves as a proton donor for the hydrogenation of CO₂. However, a drawback in this system is that the use of water shortens the electrochemical stability window (ESW) because of the parallel hydrogen evolution reaction (HER) occurring at negative potentials. 24,25 In this regard, ionic liquids (ILs) have emerged as an excellent choice for electrochemistry studies because they are room-temperature molten salts, which minimize water content and increase the ESW without inducing the HER, along with other benefits for electrochemical systems. 26-31 More specifically, ILs are being investigated for the conversion of various molecules, such as in the nitrogen reduction reaction (N2RR), which has attracted significant attention in the electrocatalysis field.³² Unlike the Haber-Bosch process, this reaction can be carried out under ambient conditions. N2 reaches a solubility of 0.28 mg per gram in [P_{6/6/6/14}][eFAP], nearly 15 times higher than its solubility in water. Moreover, a Faradaic efficiency (FE) of up to 60% was achieved using this IL for N₂RR. In terms of carbon dioxide, when coupled with the possibility of using highly negative potentials to drive the CO2RR, systems incorporating ILs can efficiently transform CO₂ into alternative products, preventing degradation and controlling the H₂ production ratio.^{33,34} Furthermore, ILs can stabilize intermediates at the catalyst surface, thereby extending their lifetime. 35-38 In this context, ILs can possibly act as stabilizers for the *CO intermediate, thereby increasing its lifetime and enhancing the production of C_{2+} molecules.

In recent years, many researchers have explored the use of ILs because of their ability to increase CO2 solubility. The most commonly used ILs are based on imidazolium cations with varying carbon chain lengths (BMIM+, EMIM+, etc.).³⁹⁻⁴² In this type of IL, a chemical bond between the cation and CO₂ is formed because of the presence of an acid site. Consequently, bond breaking is required after CO₂ reduction, entailing additional energy.⁴³ On the other hand, ILs based on other types of cations can serve solely as surface stabilizers. 44 One challenge when working with ILs is their high cost, prompting the widespread practice of adding acetonitrile (ACN) as a solvent to increase the electrolyte volume as well as to increase the CO₂ solubility, compromising the electrochemical stability of the electrolyte. Furthermore, water content is usually not controlled, complicating the understanding of how this affects product selectivity. Nevertheless, some researchers have shown that water content can indeed affect the overall behavior of systems that use ILs as electrolytes. 45,46 Additionally, water can change the physicochemical properties of ILs. 47 As a result, most publications do not distinguish the actual effects of ILs and water concentration on the CO₂ reduction mechanism.

Herein, the IL methyltributylphosphonium bis-(trifluoromethylsulfonyl)imide (P_{1444} TFSI) was selected as the electrolyte because it does not form a bond with CO_2 , has a wider ESW than aqueous electrolytes, and has high CO_2 solubility (ca. 120 mmol L^{-1}), $^{48-50}$ which is nearly four times greater than that of KHCO $_3$ (0.1 mol L^{-1}). Considering that the presence of water in the P_{1444} TFSI IL increases the CO_2 solubility, 52 the amount of water was varied to investigate which products are favored and to modulate the HER. In this case, the protons provided by water molecules are preferentially used for the hydrogenation of intermediates and

not for the formation of H_2 . Moreover, in the absence of H^+ donors, under dry conditions, the CO_2RR does not occur. The production of C_{1-4} gaseous products, H_2 , and liquid products such as $HCOOH/HCOO^-$, CH_3OH , and methyl formate could also be tuned depending on the applied potential.

■ EXPERIMENTAL SECTION

Electrode Preparation. Copper foil with 99.9% purity was employed as the substrate for the electrodeposition of Cu+ (Cu₂O). For the electrodes, the foil was cut into 5×1 cm pieces. The material was mechanically polished with 300-, 600-, and 1200-grit sandpapers, each accompanied by water. To further refine the material, an aluminum oxide suspension with 1 μ m particles was used for polishing (Arotec No. 4), and finally, water was used to wash the surface in an ultrasonic bath. Furthermore, an area of 1×1 cm was isolated for oxide deposition, representing the size of the catalyst itself. A solution of 0.3 mol L⁻¹ CuSO₄ (pentahydrate, Merck/Sigma-Aldrich) was prepared with 3 mol L-1 lactic acid (Merck/ Sigma-Aldrich), and the pH was adjusted to 12 by adding NaOH (Merck/Sigma-Aldrich) at 333 K. The electrochemical arrangement was composed of a copper foil, carbon paper (Fuel Cell Earth 50% PTFE), and a conventional Ag/ AgCl electrode with concentrated Cl⁻ as the working electrode (WE), the counter electrode (CE), and the reference electrode (RE), respectively. The interelectrode spacing between the WE and the CE was maintained in a parallel alignment and with a distance of approximately 1 to 2 cm (Figure S1). With the cell assembled, a chronopotentiometry measurement was performed by applying $-50 \mu A \text{ cm}^{-2}$ for 2 h using a Potentiostat/ Galvanostat Metrohm Autolab. After deposition, the film had an average thickness of $4 \pm 1 \mu m$ (Figure S2).

Electrode Characterization. X-ray diffraction (XRD) characterization for facet peak confirmation was performed using a Shimadzu 7000 Maxima (copper K α , λ = 1.541058 Å). Scanning electron microscopy (SEM) was performed to verify the morphology of the nanostructures using a FESEM JEOL JSM-7401F with an accelerating voltage of 10 kV, a working distance of 8 mm, and an LEI detector. For X-ray photoelectron spectroscopy (XPS), the electrodes were stored in an Ar atmosphere after electrolysis before analysis. Data were collected with a Specs instrument in fixed analyzer transmission mode, with an excitation energy of Al K α = 1486.71 eV, a detector voltage of 1800 V, and a bias voltage of 90 V. High-resolution spectra were obtained for Cu (B.E. 920-970 eV and 555-590 eV, corresponding to the Cu_{2p} and Cu_{LMM} Auger regions, respectively), O (B.E. 522–547 eV), and C (B.E. 276-298 eV). The calibration was performed at the peak of adventitious carbon C_{1s}, set to 284.8 eV. The deconvolution of the Cu_{2p} peak was performed using a Shirley baseline, with separate regions for $2p_{1/2}$ and $2p_{3/2}$, and an LA(80) line shape. Constraints on the area ratio, energy splitting, and fwhm were applied.

lonic Liquid Preparation. $[P_{1444}][TFSI]$ (Iolitec IN-0037-HP) was previously dried with a hot plate and stirred at 60 °C overnight inside an Mbraun Labmaster 130 glovebox. To work outside the argon atmosphere, a glass flask with a rubber septum was used for storage. Water was added with a syringe, piercing the septum. CO_2 was previously dried with a Gasart Humidity Filter Trigon 1/4 TTM-400-4 and bubbled for 15–20 min directly into the IL, where it saturated. A Metrohm 831 KF Coulometer was employed for titration to determine the amount of added H_2O .



Figure 1. Schematic of the setup used in this work. P_{1444} TFSI with controlled amounts of water was used as the electrolyte. Some of it was collected for 1 H NMR experiments and GC-MS, with the latter using headspace analysis to capture volatilized products. The gas from the headspace was transferred to a gas bag for further chromatographic analysis.

Electrochemical Experiments. The electrochemical cell was designed using Autodesk Fusion 360 and fabricated with a Prusa SL1 printer utilizing Anycubic ABS-Like Pro 2 resin (Figure 1). The prepared Cu₂O-deposited copper foil was used as the working electrode (WE), while two platinum wires were employed as the counter (CE) and quasi-reference (RE) electrodes. Since a pseudoreference electrode is employed in the ionic liquid (IL), its potential cannot be directly determined and must therefore be established indirectly. To achieve this, the ferrocene/ferrocenium (Fc/Fc⁺) redox couple is introduced as an electrochemically active internal standard within the electrolyte solution. By referencing the redox potential of the analyte to that of the internal standard, it becomes possible to correct for potential drift and the inherent variability associated with pseudoreference electrodes (Figure S3). This approach increases the accuracy and reproducibility of the electrochemical measurements and facilitates comparisons between publications. The WE was connected using an alligator clip and separated from the CE by a glass microfiber filter (Whatman GF/F, 125 mm, 1825-125), which served to slow the diffusion of electrochemical products toward the CE, thereby minimizing their reoxidation. Approximately 2 mL of IL was used, which was sufficient to submerge all the electrodes. To enable accurate quantification of the reaction products via proton nuclear magnetic resonance (1H NMR), the cell was weighed before and after the IL was added, allowing for precise determination of the electrolyte mass.

Cyclic voltammetry (CV) was performed to characterize the system using a Potentiostat/Galvanostat Metrohm Autolab, along with chronoamperometry measurements. The resistance of the cell was determined by Metrohm Nova positive feedback and i-interrupt tools. Since the ohmic drop values were less than 100 ohms and the current was approximately 250 μ A, no compensation was applied during the measurements once the ohmic drop approached 25 μ V. CV was conducted for catalyst electrochemical characterization with the potential starting at 0.7 V vs Fc/Fc⁺ and ranging from 0.7 to -1.2 V for a total of two to three cycles at a scan rate of 5 mV s⁻¹ (Figure S4). For electrolysis, selected potentials were applied for 3 h with the two different water concentrations, resulting in charge values close to 2-3 C. After chronoamperometry, the electrolyte was collected using a syringe, with a portion separated for NMR sample preparation and the remaining portion stored in a 2 mL vial for subsequent gas chromatography-mass spectrometry (GC-MS) identification experiments.

Product Identification and Quantification. For the liquid products, an Agilent 5977B gas chromatograph coupled with a mass spectrometry detector (MSD) and an HP1 column

was used for qualitative determination. The glass vial with the electrolyte stored was heated to 323 K to volatilize the liquid products since the IL has a vapor pressure almost equal to zero. Afterward, the headspace was collected using a 100 μ L gastight syringe (Hamilton) for manual injection. Additionally, ¹H NMR was employed to confirm the products (Figure S5 and Table S1). The electrochemical cell was weighed before and after the electrolyte was added, and the total amount of the IL was determined by the difference in mass for subsequent calculations. Quantification was performed using a Bruker 500 MHz with 256 scans using ~400 mg of electrolyte, 150 μ L of DMSO with 1% (v/v) TMS, and 20 μ L of a 125 mM phenol solution prepared in DMSO, achieving a 4 cm height in the NMR tube. The FEs of the products are described in more detail in Tables S2 and S3.

For the gaseous products, a 0.6 L Supelco Inert Foil Gas Sampling Bag was attached to the electrochemical cell, and CO₂ was used as a carrier gas to collect the headspace, achieving a volume of 75 mL. An Agilent 8860 GC System coupled with a flame ionization detector (FID) and a methanizer, as well as a thermal conductivity detector (TCD), was used for chromatography. The columns used were Agilent HP-Plot Q (80 m \times 500 μ m \times 40 μ m) for FID and CarboPLOT P7 (25 m \times 530 μ m \times 25 μ m) for TCD. The bag was connected to the gas chromatograph and pressed to fill the injection loop, delivering 1 and 0.250 mL to the FID and TCD, respectively. Quantification was accomplished using a calibration curve of known gases and their concentrations.

■ RESULTS AND DISCUSSION

Cu₂O Catalyst Characterization. To evaluate the characteristics of the pristine catalyst, XRD was conducted to identify the desired (111) facet, as depicted in Figure 2A by the peak at 36.6°. Additionally, other peaks were detected, such as (220) at 62° and (311) at 74°, along with CuO and Cu peaks.⁵³ To compare the catalyst XRD pattern with literature data, the follow reference peaks were used: for CuO, 35.6°, 38.8°, 48.9°, 58.4°, 61.8°, 66.36°, and 68.19° (JCPDS 41-0254);⁵⁴ for Cu, 43.7°, 50.7°, and 74.3° (JCPDS 04-0836);⁵⁵ and for Cu_2O , 36.33°, 42.16°, 61.47°, and 73.35° (JCPDS 05-0667).⁵⁶ SEM measurements were also used to evaluate the morphology and size of the nanoparticles, as shown in Figure 2B, revealing the coverage of the surface of the substrate and the presence of the expected octahedral structures. Finally, XPS was employed to analyze the surface species. Highresolution Cu 2p spectra (Figure 2C) showed two characteristic peaks centered at 931.4 and 951.2 eV, associated with Cu $2p_{3/2}$ and $2p_{1/2}$, respectively. These peaks can be attributed to

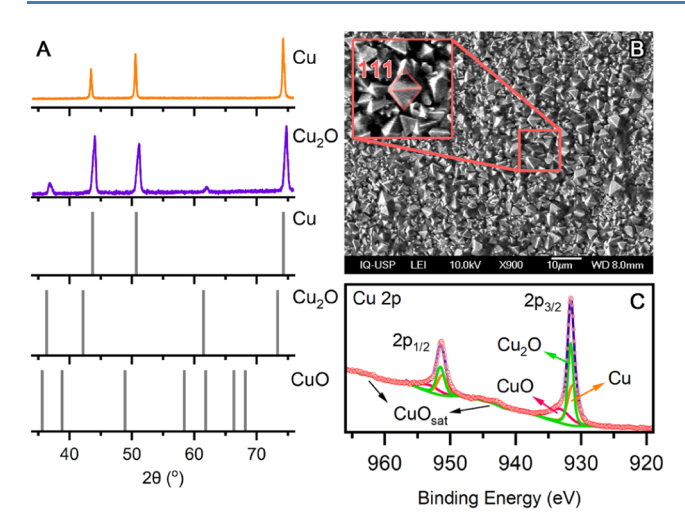


Figure 2. Catalyst characterization by (A) XRD, showing Cu_2O (blue line) and metallic copper substrate (orange line), as well as the standard peaks from the literature for Cu_2O , CuO, and Cu; (B) SEM, indicating the presence of Cu_2O octahedra covering the whole metallic copper substrate; and (C) XPS, showing the Cu 2p electrons for the catalyst before electrolysis.

either metallic copper (Cu^0) or cuprous/copper oxide (Cu^+/Cu^{2+}). S7,58 However, distinguishing between these species using Cu 2p binding energies is difficult because of their similar energy values. Additionally, no shakeup satellite peak corresponding to copper oxide (Cu^{2+}) was observed for the 2p electrons (Figure 2C). Therefore, the Auger electron region was analyzed to differentiate Cu^+ from Cu. For the prepared catalyst, before electrolysis, a distinct peak at approximately 917.2 eV is observed, indicating the presence of Cu_2O (Figure S6). Furthermore, no peaks were detected near 919 eV, which would represent Cu, while a slight shoulder appeared at approximately 918 eV, corresponding to CuO.

Electrochemical Activity of the Catalyst. The focus of this study is to demonstrate the influence of water amount on both $\rm CO_2RR$ activity and product selectivity by mitigating the HER. The results of linear sweep voltammetry (LSV) experiments recorded in $\rm P_{1444}TFSI$ electrolyte in Ar (Figure 3A) and $\rm CO_2$ (Figure 3B) atmospheres using three water concentrations (<1, 20, and 80 mmol $\rm L^{-1}$) are shown in Figure 3B. Notably, 80 mmol $\rm L^{-1}$ is the maximum amount of water that can be dissolved in $\rm P_{1444}TFSI$ before separating into two phases. When the experiment was conducted with <1 mmol $\rm L^{-1}$ water under an Ar atmosphere (yellow line in Figure 3A), almost no reduction current was observed, indicating the stability of both the electrolyte and the catalyst. As the amount

of water increased, represented by the purple and dark blue lines for 20 and 80 mmol L⁻¹ in Figure 3, respectively, the current density increased, indicating the HER and oxide reduction, although the current values remained quite low. The surface of the electrodes was analyzed by using XPS after electrolysis in an Ar atmosphere. For the systems containing 20 and 80 mmol L⁻¹ water, when -0.7 and -0.8 V vs Fc/Fc⁺ were applied, the XPS results show that the peak representing Cu⁺ remains present even after 3 h of electrolysis (Figures S7 and S8). Moreover, at more negative potentials, it is still possible to observe the presence of both Cu⁺ and Cu⁰, which is also evident from the XRD results (Figure S9). Specifically, for the 20 mmol L⁻¹ system, Cu⁺ is more prominent, suggesting the possibility of evaluating its influence on product distribution and comparing it with more negative potentials where there is more Cu⁰. This highlights the system's ability to maintain the presence of oxidized species, in contrast to aqueous systems, where Cu⁺ is typically almost fully converted to Cu⁰ after a shorter electrolysis time.⁵⁸ This opens the possibility of exploring how other metal oxides influence the CO₂RR.

The results of the experiments performed in a CO_2 atmosphere are shown in Figure 3B. When the concentration of water was <1 mmol L^{-1} (yellow line), a low current density was observed. As the water concentration increased (purple and blue lines for 20 and 80 mmol L^{-1} , respectively), a very large increase in current was observed, indicating the dependence of the CO_2RR on the presence of water. Differences in the current density scale must be noted when the data are compared in Figure 3A,B. Further negative potentials were limited to avoid H_2 production increase by water splitting and degradation of the IL.

 ${\rm CO_2}$ electroreduction necessarily requires the presence of a ${\rm H^+}$ donor, which in this case is provided by water molecules. This is evidenced by the well-known ${\rm CO_2RR}$ pathways, indicated by the following reactions: 2,4,5,9

$$2H_2O + 2e^- \rightarrow H_2 + 2OH^-$$
 (1)

$$CO_2 + H_2O + 2e^- \rightarrow CO + 2OH^-$$
 (2)

$$CO_2 + 2H_2O + 2e^- \rightarrow HCOOH + 2OH^-$$
 (3)

$$CO_2 + 6H_2O + 8e^- \rightarrow CH_4 + 8OH^-$$
 (4)

$$CO_2 + 5H_2O + 6e^- \rightarrow CH_3OH + 6OH^-$$
 (5)

$$2CO_2 + 8H_2O + 12e^- \rightarrow C_2H_4 + 12OH^-$$
 (6)

$$2CO_2 + 10H_2O + 14e^- \rightarrow C_2H_6 + 14OH^-$$
 (7)

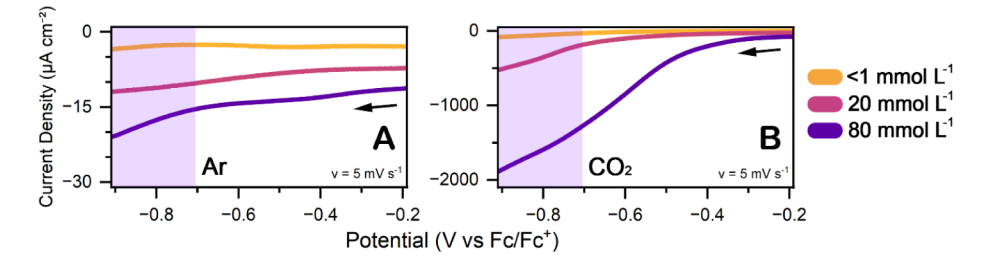


Figure 3. LSV with different water concentrations for (A) Ar and (B) CO₂. The yellow line represents <1 mmol L^{-1} water, the purple line represents 20 mmol L^{-1} , and the blue line corresponds to 80 mmol L^{-1} . All voltammetry data were recorded in P_{1444} TFSI at a scan rate of 5 mV s⁻¹. The highlighted region represents the electrolysis potential. Please note the scale of the *y*-axis.

$$3CO_2 + 12H_2O + 18e^- \rightarrow C_3H_6 + 18OH^-$$
 (8)

$$4CO_2 + 16H_2O + 24e^- \rightarrow C_4H_8 + 24OH^-$$
 (9)

$$4\text{CO}_2 + 18\text{H}_2\text{O} + 26\text{e}^- \rightarrow \text{C}_4\text{H}_{10} + 26\text{OH}^-$$
 (10)

The FEs and distributions of the different reaction products quantified by ¹H NMR and GC at various potentials and two water concentrations, i.e., 20 mmol L⁻¹ and 80 mmol L⁻¹, are shown in Figure 4. Notably, the sum of the FEs for the

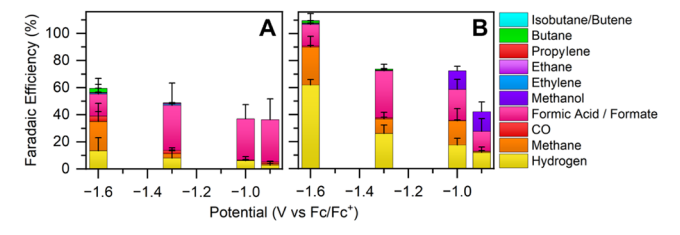


Figure 4. Faradaic efficiency at each selected potential for electrolysis with (A) 20 mmol L^{-1} and (B) 80 mmol L^{-1} water.

products at some potentials is much lower than 100%. This occurs because the reduction of the oxide effectively consumes a significant portion of the charge. This occurs because Cu₂O also needs H₂O to be reduced; therefore, some of the water molecules dissolved in the IL are also used for oxide reduction instead of the CO₂RR. This becomes more evident when LSV is conducted without CO₂ and with different concentrations of water (Figure S10). When metallic copper is used with 20 mmol L^{-1} water (represented by the curve of unfilled squares), the current density starts to drastically increase at potentials close to -2.0 V vs Fc/Fc⁺. On the other hand, when Cu₂O with the same water concentration is used, this potential is shifted to approximately -1.5 V vs Fc/Fc⁺ (purple line), indicating oxide reduction. As evidenced by the XPS results (Figures S7 and S8), for more negative potentials, more metallic copper is present in the initial catalyst, which explains why the total FE is closer to 100% at more negative potentials.

At -0.9 and -1.0 V, differences in the liquid-phase products become evident, mainly methanol and formic acid/formate, with the latter having high selectivity at 20 mmol L⁻¹ (Figure 4A). The FEs for formic acid and formate were summed because they are essentially the same molecule and can be detected at either 8.12 or 8.67 ppm (Figure S11) in the ¹H NMR spectra, respectively.

The missing FE in Figure 4A, when correlated with the peak observed in the chronoamperograms during the first 1000 s of electrolysis (Figure S12), was suspected to result from the reduction of cuprous oxide. To confirm this, another analysis was conducted after 3 h of electrolysis at -1.6 V vs Fc/Fc⁺ (Figure S13) to determine whether the peak disappeared. Indeed, the peak was no longer present, indicating its association with the oxide reduction process. The products were also quantified after this analysis, and the production of methane, which was chosen as a probe molecule, almost doubled at this potential, further indicating that the charge associated with cuprous oxide reduction had a weaker effect. Moreover, from electrochemistry of the copper oxide films in Ar (Figures S14 and S15) and XPS analyses revealed that the Cu₂O/CuO redox couple appears only above 8 mmol L⁻¹ of water, with the current increasing until stabilizing beyond 20 mmol L⁻¹. The total charge (\approx 2 mC) becomes independent of water concentration, indicating that water availability exceeds the amount required for complete CuO reduction. XPS confirmed the coexistence of Cu⁺ and Cu²⁺ species even under highly reducing conditions. Calculations further demonstrated that, at both 20 and 80 mmol L⁻¹, water is not the limiting factor for film reduction. Therefore, the increased charge observed at higher water contents under CO₂ atmosphere likely arises from the enhanced formation of hydrogenated CO₂ reduction products rather than from copper oxide reduction. Additionally, gas samples collected from the anode compartment during a CO₂ electrolysis (Figure S16) revealed no detectable CO2 reduction products, even though such species could, in principle, be reoxidized at the anode. This confirms that product crossover between the cathodic and anodic compartments did not occur, thereby eliminating potential errors in the calculation of Faradaic efficiency.

When the product distribution was compared between 80 and 20 mmol L^{-1} , as shown in Figure 5, H_2 production was consistently higher for 80 mmol L^{-1} across all potentials, as indicated by values greater than 1. Among the C_1 products, methane was significantly more prominent at 80 mmol L^{-1} when applying -1.0 V vs Fc/Fc⁺, as indicated by the orange bars. The presence of C_{2+} is detected only at higher potentials (-1.3 and -1.6 V). Additionally, among the C_{2+} products, the amounts of butane and propylene are more pronounced when the water content increases (values higher than 1) at -1.3 V and -1.6 V, respectively.

The GC-MS technique enabled the detection of methyl formate, although quantification was not feasible because of its

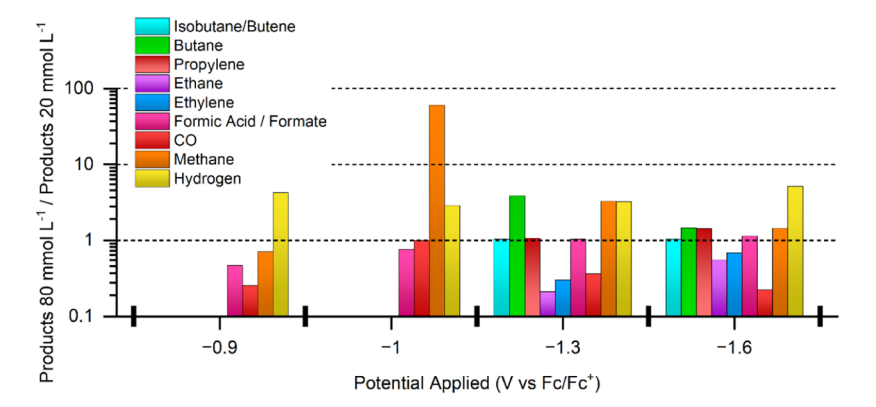


Figure 5. Relationships between the amount of each product detected at 80 and 20 mmol L^{-1} as a function of the potential.

low concentration, resulting in negligible peaks in the ¹H NMR spectrum. Furthermore, a chemical shift at 8.17 ppm is not observed for the proton from this molecule. Additionally, the shift at 3.67 ppm is indistinguishable from the signals of the IL impurities, restricting the possibility of quantification by NMR. This product is formed through the chemical reaction between methanol and formic acid (Figure S17), which has already been reported in the literature. 60 The fact that methanol formation is detected only in the system with 80 mmol L^{-1} (Figure 4B) and not in the system with 20 mmol L⁻¹ water (Figure 4A) indicates that when the amount of water is not sufficient, the pathway leading to the *CHO intermediate described in the mechanism proposed by Koper's group² does not occur or is less favorable. This hypothesis is confirmed because the CO FE increases for water concentrations of 20 mmol L⁻¹ (Figure 4A), which indicates that *CO is favored. For 80 mmol L⁻¹ (Figure 4B), this pathway is enabled, as evidenced by the formation of both methanol and methane at -1.0 V vs Fc/Fc⁺, which depends on the formation of *CHO.

The production of long carbon chains (ethylene, ethane, propylene, isobutane/butene, and butane) is observed from -1.3 V vs Fc/Fc⁺ onward. Sargent's group predicted, on the basis of calculations, that butane production depends on the dimerization of *C₂H₄₋₅ intermediates on the electrode surface, which is further enhanced by *CO coverage and the presence of soluble CO, leading to 95% selectivity for butane over 1-butene, 2-butene, and iso-butene. Additionally, two *CH₂*CO intermediates can combine, and through further hydrogenation, detach the oxygens to form butane or its isomers. With respect to these observations, the low FE for CO in Figure 4 may indicate the high coverage of the catalyst, leading to the appearance of C₂₋₄ products at more negative potentials, i.e., -1.3 and -1.6 V vs Fc/Fc⁺.

The presence of butane could also be associated with cation degradation. To discard this hypothesis, ^{31}P NMR analysis was performed on the pure IL before and after electrolysis with CO_2 at -1.6 V vs Fc/Fc^+ and 80 mmol L^{-1} water (Figure S18). The results showed essentially no new peaks, indicating that the IL remained unmodified during the experiment. Furthermore, GC-MS was performed, and butane was not detected at the expected retention time (Table S4), which confirms that the IL is not degrading (Figure S19). Finally, as shown in Figure 5, if butane production was related to IL degradation, it would likely be possible to observe an increase in its FE when more negative potentials were applied. However, this is not the case when comparing the values for -1.3 and -1.6 V vs Fc/Fc+, as the latter value is smaller.

The dimerization of ethylene intermediates can be deduced because the FE for butane is similar under both water concentrations, as shown in Figure 4A,B. This finding indicates that the amount of water does not seem to play a significant role, i.e., the reaction pathway is independent of the proton source and surface *H coverage. Since the rate-determining step for butane production is the coupling of ${}^*C_2H_{4-5}$ intermediates and is not dependent on *H, butane production arises from the previously described mechanism, which suggests that the IL either favors the binding strength of ${}^*C_2H_{4-5}$ or stabilizes the transition state. Furthermore, the detection of propylene suggests that the system favors the coupling of ${}^*C_2H_{4-5}$ with *CO , as since the dimerization pathway studied by Sargent's group produces only C_4 molecules.

CONCLUSIONS

In this work, P₁₄₄₄TFSI was successfully used as an electrolyte for the CO2RR with a Cu2O catalyst. This IL was chosen because it does not form a bond with CO2, presents a large ESW compared with aqueous electrolytes, and has a high solubility of CO₂ (ca. 120 mmol L⁻¹), almost four times higher when compared with KHCO₃ (0.1 mol L⁻¹). The amount of water was carefully controlled (<1, 20, and 80 mmol L^{-1}) to elucidate its role in tuning the CO2RR pathways and suppressing the HER. The catalyst was very active for the CO₂RR, synergizing with the electrolyte and demonstrating the ability to enhance C-C coupling at more negative potentials, as well as enhancing product selectivity. Liquid products only started to appear at -0.9 V vs Fc/Fc⁺, indicating the formation of mainly formic acid/formate and emphasizing its high selectivity when using 20 mmol L⁻¹ water, achieving 86% of the product distribution. Additionally, for this water concentration, methanol production was not detected, which indicates the absence of the *CHO intermediate, facilitating the possibility of controlling the CO2RR pathway and preferentially leading to the *CO pathway (Figure S20). Furthermore, propylene, isobutane/butene, and butane were detected at more negative potentials, i.e., -1.3 and -1.6 V vs Fc/Fc⁺, which is only possible due to the large ESW of the IL. In summary, the application of highly negative potentials effectively enhanced the CO₂ reduction reaction (CO₂RR) while simultaneously suppressing the hydrogen evolution reaction (HER), as evidenced by the consistently low Faradaic efficiency (FE) for hydrogen across all potentials in the system containing 20 mmol L⁻¹ water. Moreover, the use of 80 mmol L⁻¹ facilitated the activation of the *CHO intermediate pathway, leading to the formation of methanol and methane.

ASSOCIATED CONTENT

Supporting Information

The Supporting Information is available free of charge at https://pubs.acs.org/doi/10.1021/acscatal.5c04941.

Additional electrochemical characterization details (CV and LSV), descriptions of liquid product detection (¹H NMR), further details of electrode characterization (XPS), and more detailed faradaic efficiencies and product distributions (PDF)

AUTHOR INFORMATION

Corresponding Author

Roberto M. Torresi — Instituto de Química, Universidade de São Paulo, São Paulo, São Paulo 05508-900, Brazil; o orcid.org/0000-0003-4414-5431; Email: rtorresi@iq.usp.br

Authors

Primaggio S. Mantovi — Instituto de Química, Universidade de São Paulo, São Paulo, São Paulo 05508-900, Brazil Jean C. da Cruz — Instituto de Química, Universidade de São Paulo, São Paulo, São Paulo 05508-900, Brazil

Leonardo D. De Angelis — Instituto de Química, Universidade de São Paulo, São Paulo, São Paulo 05508-900. Brazil

Maykon L. Souza — Instituto de Química de São Carlos, Universidade de São Paulo, São Carlos, São Paulo 13566-590, Brazil

- Liane M. Rossi Instituto de Química, Universidade de São Paulo, São Paulo, São Paulo 05508-900, Brazil;
 o orcid.org/0000-0001-7679-0852
- Susana I. Córdoba de Torresi Instituto de Química, Universidade de São Paulo, São Paulo, São Paulo 05508-900, Brazil; orcid.org/0000-0003-3290-172X
- Fabio H. B. Lima Instituto de Química de São Carlos, Universidade de São Paulo, São Carlos, São Paulo 13566-590, Brazil

Complete contact information is available at: https://pubs.acs.org/10.1021/acscatal.5c04941

Author Contributions

P.S.M.: conceptualization, investigation, methodology, writing—original draft, writing—review and editing. J.C.d.C.: investigation and methodology. L.D.D.A.: investigation and methodology. M.L.S.: Investigation and methodology. L.M.R.: conceptualization, writing—review and editing. S.I.C.d.T.: conceptualization, writing—review and editing. F.H.B.L.: conceptualization, writing—review and editing. R.M.T.: conceptualization, methodology, writing—review and editing, project administration, funding acquisition, supervision.

Funding

The Article Processing Charge for the publication of this research was funded by the Coordenacao de Aperfeicoamento de Pessoal de Nivel Superior (CAPES), Brazil (ROR identifier: 00x0ma614).

Notes

The authors declare no competing financial interest.

ACKNOWLEDGMENTS

P.S.M., J.C.d.C., L.D.D.A., and M.L.S. gratefully acknowledge the São Paulo Research Foundation (FAPESP) for the fellowships granted (2021/06327-8, 2024/05899-6, 2021/ 08007-0, and 2018/10415-7). Additional support from FAPESP through Thematic Projects 2019/22183-6 and 2021/00675-4 is also acknowledged. All the authors thank the Brazilian National Council for Scientific and Technological Development (CNPq, grants 381517/2023-3, 308948/2022-0, and 406933/2021-9) and the Coordination for the Improvement of Higher Education Personnel (CAPES, grant 308948/ 2022-0) for financial support. The authors also acknowledge the support of the Research Centre for Greenhouse Gas Innovation (RCGI), hosted at the University of São Paulo (USP) and sponsored by FAPESP (grants 2020/15230-5 and 2014/50279-4) and Shell Brasil, as well as the strategic support from the Brazilian National Agency for Petroleum, Natural Gas and Biofuels (ANP) through the R&DI levy regulation. Furthermore, this research utilized facilities at the LNNANO Laboratory, which is part of the Brazilian Center for Research in Energy and Materials (CNPEM), a private, nonprofit organization supervised by the Brazilian Ministry of Science, Technology, and Innovation (MCTI). The authors also thank the XPS staff for assistance with the experiments (project 20251409). The authors acknowledge the utilization of the FAPESP Multi-User Equipment (EMU Grant 2022/15887-0). Many thanks to Dr. Eduardo Carmine (IQUSP) for his valuable help with the hydrogen electrolysis control experiments and the thickness measurements of the catalytic material formed on the copper substrate.

REFERENCES

- (1) Trends In Atmospheric Carbon Dioxide (Accessed 2 April 2025). https://gml.noaa.gov/ccgg/trends/.
- (2) Kortlever, R.; Shen, J.; Schouten, K. J. P.; Calle-Vallejo, F.; Koper, M. T. M. Catalysts and Reaction Pathways for the Electrochemical Reduction of Carbon Dioxide. *J. Phys. Chem. Lett.* **2015**, *6*, 4073–4082.
- (3) Mac Dowell, N.; Fennell, P. S.; Shah, N.; Maitland, G. C. The role of CO2 capture and utilization in mitigating climate change. *Nat. Clim. Chang.* **2017**, *7*, 243–249.
- (4) Handoko, A. D.; Wei, F.; Jenndy, J.; Yeo, B.; Seh, Z. W. Understanding heterogeneous electrocatalytic carbon dioxide reduction through operando techniques. *Nat. Catal.* **2018**, *1*, 922–934.
- (5) Kuhl, K. P.; Cave, E. R.; Abram, D. N.; Jaramillo, T. F. New insights into the electrochemical reduction of carbon dioxide on metallic copper surfaces. *Energy Environ. Sci.* **2012**, *5*, 7050–7059.
- (6) Grim, R. G.; Huang, Z.; Guarnieri, M. T.; Ferrell, J. R.; Tao, L.; Schaidle, J. A. Transforming the carbon economy: Challenges and opportunities in the convergence of low-cost electricity and reductive CO2 utilization. *Energy Environ. Sci.* **2020**, *13*, 472–494.
- (7) Hori, Y.; Wakebe, H. H. I.; Tsukamoto, T.; Koga, O. Electrocatalytic process of CO selectivity in electrochemical reduction of CO2 at metal electrodes in aqueous media. *Electrochim. Acta* **1994**, 39, 1833–1839.
- (8) Gao, J.; Choo Sze Shiong, S.; Liu, Y. Reduction of CO2 to chemicals and Fuels: Thermocatalysis versus electrocatalysis. *Chem. Eng. J.* **2023**, 472, 145033.
- (9) Kuhl, K. P.; Hatsukade, T.; Cave, E. R.; Abram, D. N.; Kibsgaard, J.; Jaramillo, T. F. Electrocatalytic conversion of carbon dioxide to methane and methanol on transition metal surfaces. *J. Am. Chem. Soc.* **2014**, *136*, 14107–14113.
- (10) Bagger, A.; Ju, W.; Varela, A. S.; Strasser, P.; Rossmeisl, J. Electrochemical CO2 Reduction: A Classification Problem. *Chem-Physchem* **2017**, *18*, 3266–3273.
- (11) Dourado, A. H. B.; da Silva, A. G. M.; Pastrián, F. A. C.; Munhos, R. L.; de Lima Batista, A. P.; de Oliveira-Filho, A. G. S.; Quiroz, J.; de Oliveira, D. C.; Camargo, P. H. C.; Córdoba de Torresi, S. I. In situ FTIR insights into the electrooxidation mechanism of glucose as a function of the surface facets of Cu2O-based electrocatalytic sensors. *J. Catal.* **2019**, 375, 95–103.
- (12) Pastrián, F. A. C.; Da Silva, A. G. M.; Dourado, A. H. B.; De Lima Batista, A. P.; De Oliveira-Filho, A. G. S.; Quiroz, J.; De Oliveira, D. C.; Camargo, P. H. C.; Córdoba De Torresi, S. I. Why Could the Nature of Surface Facets Lead to Differences in the Activity and Stability of Cu2O-Based Electrocatalytic Sensors? *ACS Catal.* 2018, 8, 6265–6272.
- (13) Möller, T.; Scholten, F.; Thanh, T. N.; Sinev, I.; Timoshenko, J.; Wang, X.; Jovanov, Z.; Gliech, M.; Roldan Cuenya, B.; Varela, A. S.; Strasser, P. Electrocatalytic CO2 Reduction on CuOx Nanocubes: Tracking the Evolution of Chemical State, Geometric Structure, and Catalytic Selectivity using Operando Spectroscopy. *Angew. Chem., Int. Ed.* **2020**, *59*, 17974–17983.
- (14) Arán-Ais, R. M.; Scholten, F.; Kunze, S.; Rizo, R.; Roldan Cuenya, B. The role of in situ generated morphological motifs and Cu(i) species in C2+ product selectivity during CO2 pulsed electroreduction. *Nat. Energy* **2020**, *5*, 317–325.
- (15) Eilert, A.; Cavalca, F.; Roberts, F. S.; Osterwalder, J.; Liu, C.; Favaro, M.; Crumlin, E. J.; Ogasawara, H.; Friebel, D.; Pettersson, L. G. M.; Nilsson, A. Subsurface Oxygen in Oxide-Derived Copper Electrocatalysts for Carbon Dioxide Reduction. *J. Phys. Chem. Lett.* **2017**, *8*, 285–290.
- (16) Cavalca, F.; Ferragut, R.; Aghion, S.; Eilert, A.; Diaz-Morales, O.; Liu, C.; Koh, A. L.; Hansen, T. W.; Pettersson, L. G. M.; Nilsson, A. Nature and distribution of stable subsurface oxygen in copper electrodes during electrochemical CO2 reduction. *J. Phys. Chem. C* **2017**, *121*, 25003–25009.
- (17) Liu, C.; Lourenço, M. P.; Hedström, S.; Cavalca, F.; Diaz-Morales, O.; Duarte, H. A.; Nilsson, A.; Pettersson, L. G. M. Stability

- and effects of subsurface oxygen in oxide-derived Cu catalyst for CO2 reduction. *J. Phys. Chem. C* **2017**, *121*, 25010–25017.
- (18) Favaro, M.; Xiao, H.; Cheng, T.; Goddard, W. A.; Yano, E. J.; Crumlin, E. J. Subsurface oxide plays a critical role in CO2 activation by Cu(111) surfaces to form chemisorbed CO2, the first step in reduction of CO2. *Proc. Natl. Acad. Sci. U. S. A.* **2017**, *114*, 6706–6711.
- (19) Fields, M.; Hong, X.; Nørskov, J. K.; Chan, K. Role of Subsurface Oxygen on Cu Surfaces for CO2 Electrochemical Reduction. *J. Phys. Chem. C* **2018**, *122*, 16209–16215.
- (20) Mahalingam, T.; Chitra, J. S. P.; Rajendran, S.; Jayachandran, M.; Chockalingam, M. J. Galvanostatic deposition and characterization of cuprous oxide thin films. *J. Cryst. Growth* **2000**, *216*, 304–310.
- (21) Jongh, P. E. D.; Vanmaekelbergh, D.; Kelly, J. J. Cu2O: Electrodeposition and Characterization. *Chem. Mater.* **1999**, *11*, 3512–3517.
- (22) Brandt, I. S.; Tumelero, M. A.; Pelegrini, S.; Zangari, G.; Pasa, A. A. Electrodeposition of Cu2O: growth, properties, and applications. *J. Solid State Electrochem.* **2017**, 21, 1999–2020.
- (23) Golden, T. D.; Shumsky, M. G.; Zhou, Y.; VanderWerf, R. A.; Van Leeuwen, R. A.; Switzer, J. A. Electrochemical Deposition of Copper(I) Oxide Films. *Chem. Mater.* **1996**, *8*, 2499–2504.
- (24) Martins, V. L.; Mantovi, P. S.; Torresi, R. M. Suppressing early capacitance fade of electrochemical capacitors with water-in-salt electrolytes. *Electrochim. Acta* **2021**, 372, 137854.
- (25) Yokoyama, Y.; Fukutsuka, T.; Miyazaki, K.; Abe, T. Origin of the Electrochemical Stability of Aqueous Concentrated Electrolyte Solutions. *J. Electrochem. Soc.* **2018**, *165*, A3299–A3303.
- (26) Hayyan, M.; Mjalli, F. S.; Hashim, M. A.; AlNashef, I. M.; Mei, T. X. Investigating the electrochemical windows of ionic liquids. *J. Ind. Eng. Chem.* **2013**, *19*, 106–112.
- (27) Neubauer, S. S.; Krause, R. K.; Schmid, B.; Guldi, D. M.; Schmid, G. Overpotentials and Faraday Efficiencies in CO2 Electrocatalysis-the Impact of 1-Ethyl-3-Methylimidazolium Trifluoromethanesulfonate. *Adv. Energy Mater.* **2016**, *6*, 1502231.
- (28) Macfarlane, D. R.; Tachikawa, N.; Forsyth, M.; Pringle, J. M.; Howlett, P. C.; Elliott, G. D.; Davis, J. H.; Watanabe, M.; Simon, P.; Angell, C. A. Energy applications of ionic liquids. *Energy Environ. Sci.* **2014**, *7*, 232–250.
- (29) Lei, Z.; Chen, B.; Koo, Y. M.; Macfarlane, D. R. Introduction: Ionic Liquids. *Chem. Rev.* **2017**, *117*, 6633–6635.
- (30) Matuszek, K.; Piper, S. L.; Brzęczek-Szafran, A.; Roy, B.; Saher, S.; Pringle, J. M.; MacFarlane, D. R. Unexpected Energy Applications of Ionic Liquids. *Adv. Mater.* **2024**, *36*, 2313023.
- (31) Macfarlane, D. R.; Forsyth, M.; Howlett, P. C.; Pringle, J. M.; Sun, J.; Annat, G.; Neil, W.; Izgorodina, E. I. Ionic liquids in electrochemical devices and processes: Managing interfacial electrochemistry. *Acc. Chem. Res.* **2007**, *40*, 1165–1173.
- (32) Zhou, F.; Azofra, L. M.; Ali, M.; Kar, M.; Simonov, A. N.; McDonnell-Worth, C.; Sun, C.; Zhang, X.; Macfarlane, D. R. Electrosynthesis of ammonia from nitrogen at ambient temperature and pressure in ionic liquids. *Energy Environ. Sci.* **2017**, *10*, 2516–2520.
- (33) Ratschmeier, B.; Paulsen, C.; Stallberg, K.; Roß, G.; Daum, W.; Pöttgen, R.; Braunschweig, B. Cu/Au(111) Surfaces and AuCu Intermetallics for Electrocatalytic Reduction of CO2 in Ionic Liquid Electrolytes. ACS Catal. 2024, 14, 1773–1784.
- (34) Zarandi, R. F.; Rezaei, B.; Ghaziaskar, H. S.; Ensafi, A. A. Electrochemical reduction of CO2 to ethanol using copper nanofoam electrode and 1-butyl-3-methyl-imidazolium bromide as the homogeneous co-catalyst. *J. Environ. Chem. Eng.* **2019**, *7*, 103141.
- (35) Dupont, J.; Suarez, P. A. Z. Physico-chemical processes in imidazolium ionic liquids. *Phys. Chem. Chem. Phys.* **2006**, *8*, 2441–2452.
- (36) Shkrob, I. A.; Wishart, J. F. Charge trapping in imidazolium ionic liquids. *J. Phys. Chem. B* **2009**, *113*, 5582–5592.
- (37) Yang, D.; Zhu, Q.; Han, B. Electroreduction of CO2 in Ionic Liquid-Based Electrolytes. *Innov* **2020**, *1*, 100016.

- (38) Zanatta, M.; Simon, N. M.; Dupont, J. The Nature of Carbon Dioxide in Bare Ionic Liquids. *ChemSuschem* **2020**, *13*, 3101–3109.
- (39) Lim, H.-K.; Kwon, Y.; Kim, H. S.; Jeon, J.; Kim, Y.-H.; Lim, J.-A.; Kim, B.-S.; Choi, J.; Kim, H. Insight into the Microenvironments of the Metal–Ionic Liquid Interface during Electrochemical CO2 Reduction. *ACS Catal.* **2018**, *8*, 2420–2427.
- (40) Guo, W.; Liu, S.; Tan, X.; Wu, R.; Yan, X.; Chen, C.; Zhu, Q.; Zheng, L.; Ma, J.; Zhang, J.; Huang, Y.; Sun, X.; Han, B. Highly Efficient CO2 Electroreduction to Methanol through Atomically Dispersed Sn Coupled with Defective CuO Catalysts. *Angew. Chem., Int. Ed.* **2021**, *60*, 21979–21987.
- (41) Dongare, S.; Coskun, O. K.; Cagli, E.; Lee, K. Y. C.; Rao, G.; Britt, R. D.; Berben, L. A.; Gurkan, B. A Bifunctional Ionic Liquid for Capture and Electrochemical Conversion of CO2 to CO over Silver. *ACS Catal.* **2023**, *13*, 7812–7821.
- (42) Rosen, B. A.; Salehi-Khojin, A.; Thorson, M. R.; Zhu, W.; Whipple, D. T.; Kenis, P. J. A.; Masel, R. I. Ionic Liquid Mediated Selective Conversion of CO2 to CO at. *Science* **2011**, 334, 643–644.
- (43) Vasilyev, D. V.; Shyshkanov, S.; Shirzadi, E.; Katsyuba, S. A.; Nazeeruddin, M. K.; Dyson, P. J. Principal Descriptors of Ionic Liquid Co-catalysts for the Electrochemical Reduction of CO2. *ACS Appl. Energy Mater.* **2020**, *3*, 4690–4698.
- (44) Faggion, D.; Gonçalves, W. D. G.; Dupont, J. CO2 electroreduction in ionic liquids. *Front. Chem.* **2019**, *7*, 102.
- (45) Papasizza, M.; Yang, X.; Cheng, J.; Cuesta, A. Electrocatalytic reduction of CO2 in neat and water-containing imidazolium-based ionic liquids. *Curr. Opin. Electrochem.* **2020**, *23*, 80–88.
- (46) Yuan, L.; Zhang, L.; Feng, J.; Jiang, C.; Feng, J.; Li, C.; Zeng, S.; Zhang, X. Upscaling studies for efficiently electric-driven CO2 reduction to CO in ionic liquid-based electrolytes. *Chem. Eng. J.* **2022**, *450*, 138378.
- (47) Martins, V. L.; Nicolau, B. G.; Urahata, S. M.; Ribeiro, M. C. C.; Torresi, R. M. Influence of the water content on the structure and physicochemical properties of an ionic liquid and its Li+ mixture. *J. Phys. Chem. B* **2013**, *117*, 8782–8792.
- (48) Sánchez-Ramírez, N.; Assresahegn, B. D.; Bélanger, D.; Torresi, R. M. A Comparison among Viscosity, Density, Conductivity, and Electrochemical Windows of N-n-Butyl-N-methylpyrrolidinium and Triethyl-n-pentylphosphonium Bis(fluorosulfonyl imide) Ionic Liquids and Their Analogues Containing Bis(trifluoromethylsulfonyl) Imide. J. Chem. Eng. Data 2017, 62, 3437–3444.
- (49) Seo, S.; Desilva, M. A.; Xia, H.; Brennecke, J. F. Effect of Cation on Physical Properties and CO2 Solubility for Phosphonium-Based Ionic Liquids with 2-Cyanopyrrolide Anions. *J. Phys. Chem. B* **2015**, *119*, 11807–11814.
- (50) Follador, L. K.; Pereira, R. G.; Mantovi, P. S.; Siqueira, L. J. A.; Torresi, R. M. Computational evaluation of phosphonium ILs as CO2 absorbents for electrochemistry. *J. Mol. Liq.* **2024**, *415*, 126431.
- (51) Li, J.; Guo, J.; Dai, H. Probing dissolved CO2(aq) in aqueous solutions for CO2 electroreduction and storage. *Sci. Adv.* **2022**, 8, No. eabo0399.
- (52) Taylor, S. F. R.; McCrellis, C.; McStay, C.; Jacquemin, J.; Hardacre, C.; Mercy, M.; Bell, R. G.; De Leeuw, N. H. CO2 capture in wet and dry superbase ionic liquids. *J. Solution Chem.* **2015**, *44*, 511–527.
- (53) Li, C.; Li, Y.; Delaunay, J. J. A novel method to synthesize highly photoactive Cu2O microcrystalline films for use in photoelectrochemical cells. ACS Appl. Mater. Interfaces 2014, 6, 480–486.
- (54) Rakshit, S.; Mondal, K. G.; Jana, P. C.; Kamilya, T.; Saha, S. Structural and optical properties of chemically synthesized copper oxide nanoparticles and their photocatalytic application. *J. Mater. Sci.: Mater. Electron.* **2023**, *34*, 2141.
- (55) Fikry, M.; Tawfik, W.; Omar, M. M. Investigation on the effects of laser parameters on the plasma profile of copper using picosecond laser induced plasma spectroscopy. *Opt. Mater. Express.* **2020**, *52*, 249. (56) Fodor, S.; Baia, L.; Baán, K.; Kovács, G.; Pap, Z.; Hernadi, K.
- The effect of the reducing sugars in the synthesis of visible-light-active copper(I) oxide photocatalyst. *Molecules* **2021**, *26*, 1149.

- (57) Herzog, A.; Bergmann, A.; Jeon, H. S.; Timoshenko, J.; Kühl, S.; Rettenmaier, C.; Lopez Luna, M.; Haase, F. T.; Roldan Cuenya, B. Operando Investigation of Ag-Decorated Cu2O Nanocube Catalysts with Enhanced CO2 Electroreduction toward Liquid Products. *Angew. Chem., Int. Ed.* **2021**, *60*, 7426–7435.
- (58) Permyakova, A. A.; Herranz, J.; El Kazzi, M.; Diercks, J. S.; Povia, M.; Mangani, L. R.; Horisberger, M.; Patru, A.; Schmidt, T. J. On the Oxidation State of Cu2O upon Electrochemical CO2 Reduction: An XPS Study. *ChemPhyschem* **2019**, 20, 3120–3127.
- (59) Jung, H.; Lee, S. Y.; Lee, C. W.; Cho, M. K.; Won, D. H.; Kim, C.; Oh, H. S.; Min, B. K.; Hwang, Y. J. Electrochemical Fragmentation of Cu 2 O Nanoparticles Enhancing Selective C-C Coupling from CO 2 Reduction Reaction. *J. Am. Chem. Soc.* **2019**, *141*, 4624–4633.
- (60) Khan, Z.; Javed, F.; Shamair, Z.; Hafeez, A.; Fazal, T.; Aslam, A.; Zimmerman, W. B.; Rehman, F. Current developments in esterification reaction: A review on process and parameters. *J. Ind. Eng. Chem.* **2021**, *103*, 80–101.
- (61) Lee, M. G.; Li, X. Y.; Ozden, A.; Wicks, J.; Ou, P.; Li, Y.; Dorakhan, R.; Lee, J.; Park, H. K.; Yang, J. W.; et al. Selective synthesis of butane from carbon monoxide using cascade electrolysis and thermocatalysis at ambient conditions. *Nat. Catal.* **2023**, *6*, 310–318
- (62) Rihm, S. D.; Kovalev, M. K.; Lapkin, A. A.; Ager, J. W.; Kraft, M. On the role of C4 and C5 products in electrochemical CO2 reduction via copper-based catalysts. *Energy Environ. Sci.* **2023**, *16*, 1697–1710.

